Chinese Society of Aeronautics and Astronautics
& Beihang University

Chinese Journal of Aeronautics

cja@buaa.edu.cn
www.sciencedirect.com

Fracture behavior and self-sharpening mechanisms of polycrystalline cubic boron nitride in grinding based on cohesive element method

Xin HUANG [a], Haonan LI [b], Zhiwen RAO [a], Wenfeng DING [a],*

[a] College of Mechanical and Electrical Engineering, Nanjing University of Aeronautics and Astronautics, Nanjing 210016, China
[b] School of Aerospace, The University of Nottingham Ningbo China, Ningbo 315100, China

Abstract Unlike monocrystalline cubic boron nitride (CBN), polycrystalline CBN (PCBN) shows not only higher fracture resistance induced by tool-workpiece interaction but also better self-sharpening capability; therefore, efforts have been devoted to the study of PCBN applications in manufacturing engineering. Most of the studies, however, remain qualitative due to difficulties in experimental observations and theoretical modeling and provide limited in-depth understanding of the self-sharpening behavior/mechanism. To fill this research gap, the present study investigates the self-sharpening process of PCBN abrasives in grinding and analyzes the macro-scale fracture behavior and highly localized micro-scale crack propagation in detail. The widely employed finite element (FE) method, together with the classic Voronoi diagram and cohesive element technique, is used considering the pronounced success of FE applications in polycrystalline material modeling. Grinding trials with careful observation of the PCBN abrasive morphologies are performed to validate the proposed method. The self-sharpening details, including fracture morphology, grinding force, strain energy, and damage dissipation energy, are studied. The effects of maximum grain cut depths (MGCDs) and grinding speeds on the PCBN fracture behavior are discussed, and their optimum ranges for preferable PCBN self-sharpening performance are suggested.

1. Introduction

Cubic boron nitride (CBN), as the second hardest material after diamond, has been increasingly used in the ultra-high-precision manufacturing industry due to its superior thermal stability and relatively low cost. Thus, CBN tools are considered to have promising abrasive properties, especially for difficult-to-cut materials with low thermal conductivity and high toughness, such as titanium alloy and nickel-based

* Corresponding author.
  E-mail address: dingwf2000@vip.163.com (W. DING).
Peer review under responsibility of Editorial Committee of CJA.

Production and hosting by Elsevier

superalloy, which are used in aerospace engineering.[1–5] CBN abrasives can be categorized into two groups, namely, monocrystalline CBN (MCBN) and polycrystalline CBN (PCBN). Unlike MCBN, PCBN shows not only higher resistance to fracture induced by tool–workpiece interaction (due to the isotropic microstructure and mechanical properties) but also better self-sharpening capability (owing to the substantial crystalline boundaries within the microcrystalline CBN).[6,7] Thus, extensive efforts have been devoted to the study of PCBN applications in manufacturing engineering.

A pioneering study related to PCBN abrasive tools was the creation of a single-layer brazed PCBN superabrasive wheel. Ding et al.[8] brazed the PCBN abrasives onto the wheel substrate with a Cu–Sn–Ti alloy and then studied the influences of brazing temperature and holding time on the elemental distribution, abrasive fracture behavior, and interfacial microstructure of the obtained tools. Chen et al.[9] performed grinding trials of TC4 by separately using wheels with single-layer PCBN and MCBN and found that the PCBN resulted in a higher material removal rate and less grain wear. Miao et al.[10] conducted similar comparison trials by performing the grinding for a nickel-based superalloy and found that the micro fracture of the PCBN abrasive was more dominant than the macro fracture and abrasion wear during grinding; this condition could be experimentally evidenced by the fractal dimension comparison of the reconstructed 3D abrasive profile before and after the trials. Zhu et al.[11] explored the influences of bonding materials, embedding depth, gap thickness, and grain size on the distribution of residual stress in a brazed PCBN grain by establishing a finite element (FE) model; they concluded that the largest tensile stress could be obtained at the grain-bond junction region regardless of the bonding material and grain embedding depth.

Despite the availability of several studies that have provided fundamental knowledge, an in-depth understanding of the PCBN abrasive grain facture behavior during the grinding process is necessary, especially when aiming to fully explore the superior self-sharpening capability of PCBN due to its micro fracture behavior during grinding. Research[9,12–16] has proven the outstanding self-sharpening capability and superior grinding performance of wheels with PCBN abrasives; however, most studies remain qualitative due to the difficulties in experimental observations of micro-scale fractures and theoretical modeling of random brittle crack propagation and complex grain–workpiece interactions. To the best knowledge of the authors, very limited understanding has been provided on the self-sharpening process of PCBN abrasives with in-depth details (e.g., force history, fracture morphology evolution, and residual tensile stress/strain energy within the abrasive bodies[17,18]), let alone the effects of grinding parameters on the self-sharpening behavior.

However, investigating the self-sharpening process of the PCBN abrasive grain only through grinding trials is extremely difficult and time-consuming due to its weakness in controlling the experimental parameters precisely, especially for the same grain microstructures in trials with different grinding parameters. In the past decades, related numerical methods have been widely applied to solve similar problems with the rapid development of computational science. Among all numerical approaches, FE method (FEM), together with the developed cohesive element model, has been one of the most extensively used methods in the research on material behavior, especially

for brittle and ductile materials, with focus on stress singularity analysis and crack propagation[19,20]. Hillerborg[21] and Needleman[22] separately introduced fracture mechanics to study the fracture behavior of brittle and ductile materials by coupling the cohesive element model with the classic FE scheme. Zhou et al.[23] used the cohesive element method to explore the effects of grain size, grain boundary strength, and microcracks of ceramic tool materials on crack patterns and fracture toughness. Seyedeh et al.[24] investigated the influences of microstructural parameters on the strength and toughness of silicon nitride by employing the dynamic cohesive elements in the classic FE model, and thus the transgranular and intergranular crack behavior could be simulated. The fracture mechanisms of polycrystalline alumina were explored by Wang[25] with the applied cohesive element method and micromechanical tests at a grain level, and the results showed that the crystalline morphology and orientation of grains significantly influenced the localized stress inside the polycrystalline alumina.

To this end, this study investigates the self-sharpening process of PCBN abrasives in grinding, and detailed macro-scale fracture behavior and highly localized micro-scale crack propagation analyses are provided. The widely employed FEM, together with the classic Voronoi diagram (VD)[26] and the cohesive element technique, is used considering the success of FE applications in the field of polycrystalline material modeling[27–29]. Grinding trials with careful observation of the PCBN abrasive morphologies are performed to validate the proposed method. The self-sharpening details, including fracture morphology, grinding force, strain energy, and damage dissipation energy, are studied using the validated methodology. The effects of maximum grain cut depths (MGCDs) and grinding speeds on the PCBN fracture behavior are discussed, and their optimum ranges for preferable PCBN self-sharpening performance are suggested.

2. FE model for fracture analysis of PCBN abrasives in grinding

2.1. Crystalline modeling of PCBN abrasives based on VD

PCBN is a typical polycrystalline material (see Fig. 1(a)) that can be synthesized by using microcrystalline CBN particles and AlN binders in a high-temperature and high-pressure environment[30,31]. Considering the high similarity between the microstructure of polycrystalline materials[32–35] and the geometric characteristics of VD, VD is employed in this study to describe the crystalline structure of PCBN abrasives.

VD is a method that can divide a finite spatial domain into small unit areas (called Voronoi cells) and then update each cell boundary by merging or subdividing the cells on the basis of certain conditions (see Fig. 1(b)). Each cell is initially defined by its geometrical center (called seed point) and all other discrete points surrounding the center (called boundary points).[36] In VD theory, crystals are usually depicted by a set of seed points, and each point corresponds to a certain Voronoi cell, which represents a single crystalline cell in polycrystalline materials. The Voronoi cell can be mathematically described by a set (R_k) as in Eq.(1) when assuming that $d(x, A) = \inf \{d(x,a)|a \in A\}$ can represent the distance between point $\times$ and subset A.

$$R_k = \{x \in X | d(x, P_k) \leq d(x, P_j) \text{ for all } j \neq k\} \quad (1)$$

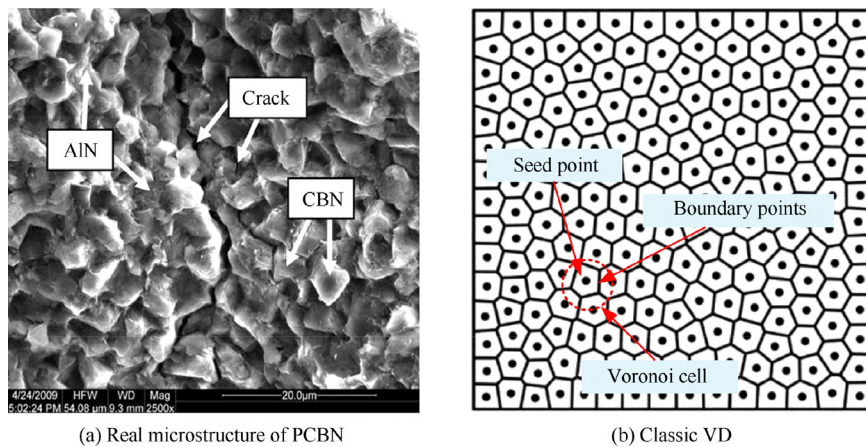(a) Real microstructure of PCBN (b) Classic VD

Fig. 1 Comparison between PCBN and VD.

where X is the defined spatial domain, d is the distance function defined in X, K is the index set, $P_{k(k\in K)}$ is the seed point that belongs to X, R_k is the point set that corresponds to P_k, and $P_{j(j\neq k)}$ is a random point defined in X.

In this study, the VD modeling of PCBN abrasives is performed by the following three steps:

(i) Geometrically describing an arbitrary convex 3D shape of PCBN abrasive

The 3D shape may contain multiple planes, and each of them is expressed by the equation with the form of $a_0x + b_0y + c_0z = d$, where (a_0, b_0, c_0) is the plane normal vector.

(ii) Determining the Voronoi cell number based on PCBN abrasive and microcrystalline CBN sizes

The area of any single plane of PCBN abrasive is assumed to be S and the diameter of microcrystalline CBN particle to be d_0; the number of Voronoi cells (N) can be represented as[37]

$$N = \frac{4S}{\pi d_0^2} \qquad (2)$$

(iii) Importing the VD data of the PCBN abrasives, including the geometric parameters obtained in (i) and the Voronoi cell number achieved in (ii), into the FE package (e.g., ABAQUS).

The geometric model of PCBN abrasives is simplified as a square plate with a size of 50 μm × 50 μm × 10 μm. This simplification is due to the article's scope, which is on the PCBN fracture behavior during the real grinding stage, in which the sharp cutting edges (see Fig. 2(a)) might be lost due to the intensive grain–workpiece interaction, during which worn flat emerges (see Fig. 2(b) and (c)). v_s denotes the grinding speed and v_w denotes the workpiece in-feed speed.

The VD grain model in this study contains 30 Voronoi cells (see Fig. 3(a)) because the diameter of microcrystalline CBN particle is approximately 10 μm (Zhengzhou Zhongnan Jete Superabrasives Co., Ltd.) and the corresponding area of each

grain plane is 50 μm × 50 μm (calculated according to Eq. (2)). Each cell is expected to represent a microcrystalline CBN particle (see Fig. 3(b)).

2.2. Fracture behavior description based on cohesive element theory

In this study, the PCBN fracture behavior is depicted by using the classic FE scheme through the explicit formulation based on cohesive element theory.

Cohesive element theory, developed by Dugdale[38] and Barenblett,[39] has been widely used to study the crack propagation behavior of brittle and ductile polycrystalline materials. In this method, a single layer of cohesive elements with finite thickness is embedded between two neighboring meshed FE elements (or micro components), as shown in Fig. 4(a), and all the layers of cohesive elements constitute the cohesive zone. The cohesive zone can be treated as an adhesive material with continuum macroscopic properties. The constitutive responses of the cohesive elements when simulating the crack propagation behavior are calculated on the basis of the traction–separation law (t-δ law) (see Fig. 4(c)) according to the material properties. From the material mechanics,[40] the cohesive elements should have three traction–separation directions (see Fig. 4 (b)), namely, (i) normal traction–separation (t_n-δ_n), (ii) first shear traction–separation (t_s-δ_s), and (iii) second shear traction–separation (t_t-δ_t).

The traction–separation law generally consists of three fundamental parameters, namely, (i) tensile strength T_{max} (material property), (ii) initial fracture toughness K_c (VD model parameter), and (iii) fracture energy G_c. And the fracture energy G_c can be determined by the elasticity modulus E and the fracture toughness K_c, as described in Eq. (3).[41]

$$G_c = \frac{K_c^2}{E} \qquad (3)$$

According to the traction–separation law, the fracture process of brittle materials includes three stages, namely, (i) linearly elastic stage, (ii) fracture initiation stage (initialization corresponding to critical data point (δ^0, t^0), as depicted in Fig. 4(c)), and (iii) fracture evolution stage.
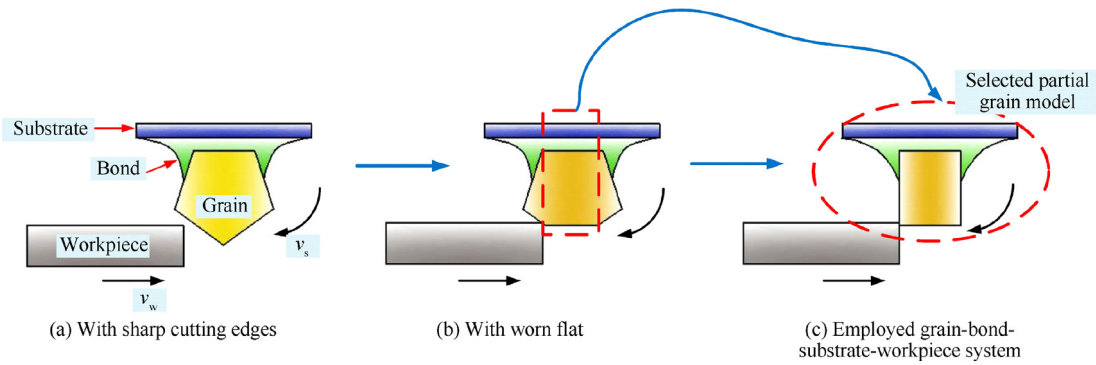
(a) With sharp cutting edges

(b) With worn flat

(c) Employed grain-bond-substrate-workpiece system

Fig. 2   Schematic of grain–workpiece interaction during grinding.

(a) VD model of PCBN grain

(b) Microstructural graph of PCBN grain

Fig. 3   Similar features of VD model and microstructural graph of PCBN grain.

(a) Embedding cohesive elements

(b) Mechanical analysis of cohesive elements

(c) Traction-separation law

(d) Linearly elastic stage

(e) Fracture initiation stage

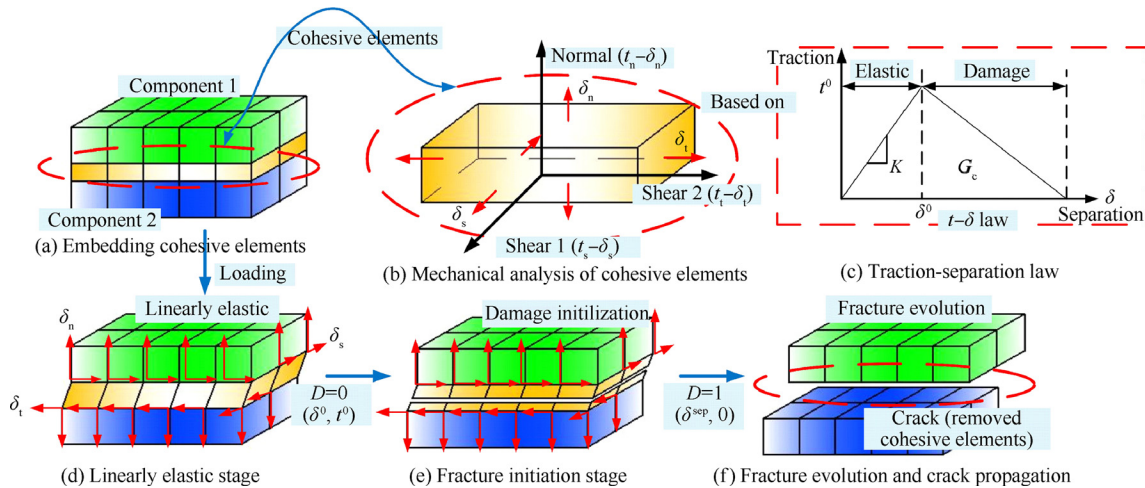(f) Fracture evolution and crack propagation

Fig. 4   Schematic of cohesive element theory applied in fracture behavior simulation.

(i) Linearly elastic stage

In the linearly elastic stage (see Fig. 4(d)), the element behavior can be described by the elastic constitutive matrix relating the normal stresses to the nominal strains across the interface, i.e.,

$$
\boldsymbol{t} = \begin{bmatrix} t_n \\ t_s \\ t_t \end{bmatrix} = \begin{bmatrix} E_{nn} & E_{ns} & E_{nt} \\ E_{ns} & E_{ss} & E_{st} \\ E_{nt} & E_{st} & E_{tt} \end{bmatrix} \begin{bmatrix} \varepsilon_n \\ \varepsilon_s \\ \varepsilon_t \end{bmatrix} = \boldsymbol{E\varepsilon} \tag{4}
$$

where $\boldsymbol{t}$ is the 3D nominal stress vector that consists of the normal component t_n and the two shear tractions t_s and t_t; $\boldsymbol{E}$ is the
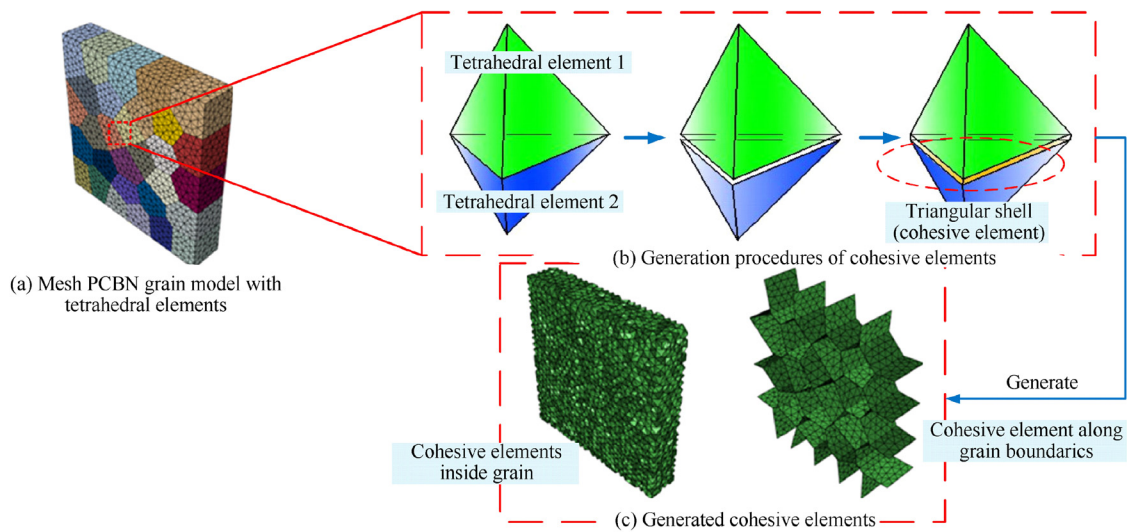
Fig. 5   Basic procedures of embedding cohesive elements into PCBN grain geometry model.

Table 1   Material parameters of PCBN abrasive grain.

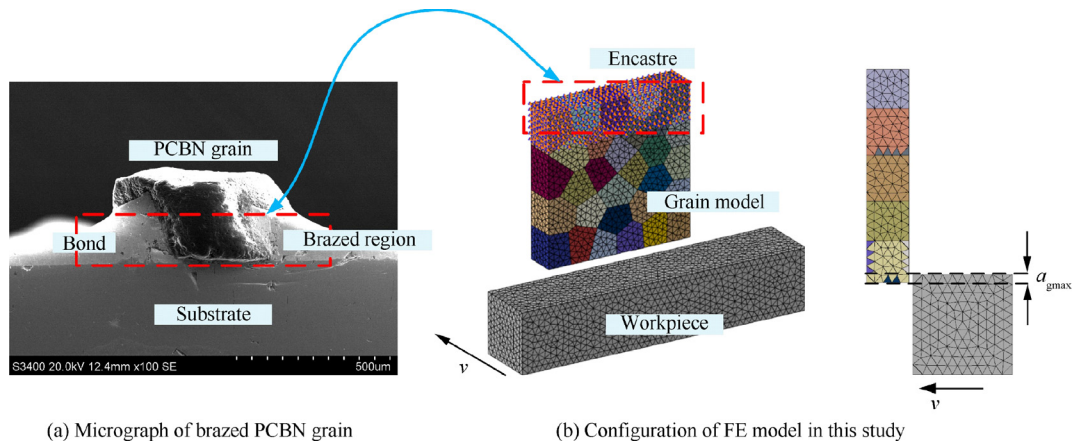| Elements in model	Young's modulus E (GPa)	Poisson ratio υ	Tensile strength T_{max} (MPa)	Fracture energy G_c (J/m^2)
Tetrahedral elements (CBN)	909	0.12		
Cohesive element in grains			2000	0.084
Cohesive element along grain boundaries			1200	0.059

Fig. 6   Schematic of FE model employed in this study.

Table 2   Boundary conditions employed in this study.

Parameter	Value
MGCD a_{gmax} (µm)	0.2, 0.4, 0.6, 0.8, 1.0 (when v_s = 40 m/s)
Grinding speed v_s (m/s)	20, 30, 40, 60, 80 (when a_{gmax} = 0.2 µm)

elastic constitutive matrix; $\boldsymbol{\varepsilon}$ is the nominal strain vector, which can be defined as

$$\boldsymbol{\varepsilon} = \begin{bmatrix} \varepsilon_n \\ \varepsilon_s \\ \varepsilon_t \end{bmatrix} = \begin{bmatrix} \frac{\delta_n}{T_o} \\ \frac{\delta_s}{T_o} \\ \frac{\delta_t}{T_o} \end{bmatrix} \qquad (5)$$

where δ_n, δ_s, and δ_t are the corresponding separations, and T_o is the original thickness of the cohesive element.

(ii) Fracture initiation stage

Table 3 Material properties of employed nickel-based super-alloy (Inconel 718).

Property	Value
Density (kg/mm^3)	8.47×10^{-6}
Young's modulus (GPa)	206
Poisson ratio	0.3
Conductivity (W/(m·K))	11.2
Thermal expansion coefficient	1.5×10^{-5}
Specific heat (J/(kg·K))	203

When the maximum nominal stress ratio is larger than the critical value (see Eq. (6)), the damage occurs according to the damage evolution law, and the fracture then initiates (see Fig. 4(e)).

$$\max\{\frac{<t_n>}{t_n^o}, \frac{t_s}{t_s^o}, \frac{t_t}{t_t^o}\} = 1 \qquad (6)$$

where t_n^o, t_s^o, and t_t^o represent the peak stress values in the normal, first, and second shear directions, respectively, when the deformation is purely normal to the interface. The Macaulay bracket refers to the pure compressive deformation or stress state that would not result in any damage initiation.

(iii) Fracture evolution stage

The scalar damage variable D describes the fracture evolution stage, where D varies from 0 to 1 on the basis of the loading/unloading conditions to capture the combined effects of all possible crack propagation mechanisms. The development of each stress component can then be expressed as

$$\begin{cases} t_n = \begin{cases} (1-D)\,\bar{t}_n & \bar{t}_n \geq 0 \\ \bar{t}_n & \text{otherwise (no damage to compressive stiffness)} \end{cases} \\ t_s = (1-D)\,\bar{t}_s \\ t_t = (1-D)\,\bar{t}_t \end{cases} \qquad (7)$$

where $\bar{t}_n$, $\bar{t}_s$, and $\bar{t}_t$ are the original stress components without consideration of any damage evolution effect.

The material failure happens if D reaches the value of one (corresponding to the fracture evolution point (δ^{sep}, 0)), and then the cohesive elements would be removed, which indicates that the cracks propagate along the bulk material (see Fig. 4 (f)).

Multitudes of triangular cohesive elements are created by several steps through the script written in Python to simulate the intergranular and transgranular fractures of PCBN abrasives. First, the PCBN abrasive geometry is meshed by tetrahedral elements (see Fig. 5(a)). Second, similar triangle planes parallel to the shared plane between any two adjacent tetrahedral elements with a finite thickness are formed (see Fig. 5(b)). Third, the three nodes of the newly created triangle plane are defined as the three points of the triangular cohesive elements. The desired cohesive elements set along grain boundaries are used to simulate the intergranular fracture behavior, and the inside elements are for the transgranular fracture behavior (see Fig. 5(c)). The material properties of the cohesive elements within the grain are set to be the same as those of microcrystalline CBN particles, and those along the grain boundaries are the same as those of the AlN binders[42] (see Table 1).
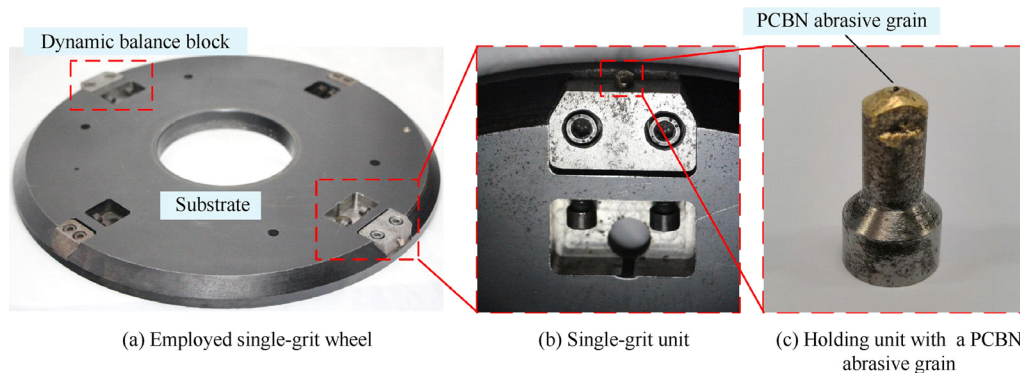
2.3. Boundary conditions

For the monolayer PCBN wheels, the abrasives are usually firmly fixed on the wheel substrate by brazing half of the abrasive volume onto the wheel surface (see Fig. 6(a)), and thus the full constraint with six degrees of freedom is applied to the fixed half volume. The translational velocity (or the load) is imposed on the workpiece, and the abrasive–workpiece overlapping depth is set to be MGCD (this value will be properly controlled in the single-grit grinding trials in the following part to be comparable) to simulate the real PCBN grain–workpiece interaction (see Fig. 6(b)). The employed boundary conditions are presented in Table 2. The workpiece is assumed to be a rigid body because the paper scope focuses on the PCBN fracture process and self-sharpening characteristics.

3. Experiments

In recent years, single-grit grinding trials have been carried out widely to study the material removal mechanism and abrasive grain wear.[43–47] In the current work, it is conducted not only to validate the proposed FE methodology but also to investigate the fracture behavior of the PCBN abrasive grain under different grinding conditions.

3.1. Experimental setup

Nickel-based superalloy (Inconel 718) blocks with a dimension of 100 mm (length) × 50 mm (width) × 10 mm (height) are used as the workpiece, and their material properties are pre-

(a) Employed single-grit wheel   (b) Single-grit unit   (c) Holding unit with a PCBN abrasive grain

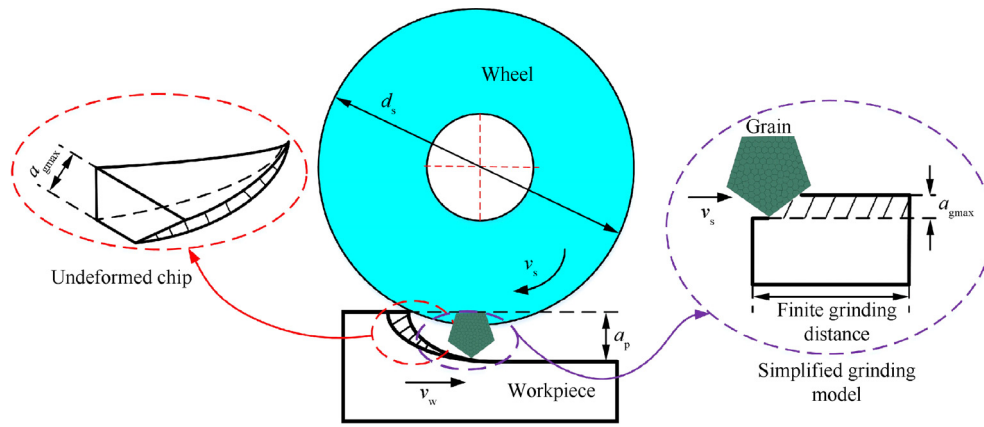**Fig. 7** Schematic of experimental setup.

Fig. 8 Schematic of MGCD and illustration of simplified grinding model relating to a_{gmax}.

Table 4 Employed grinding parameters.

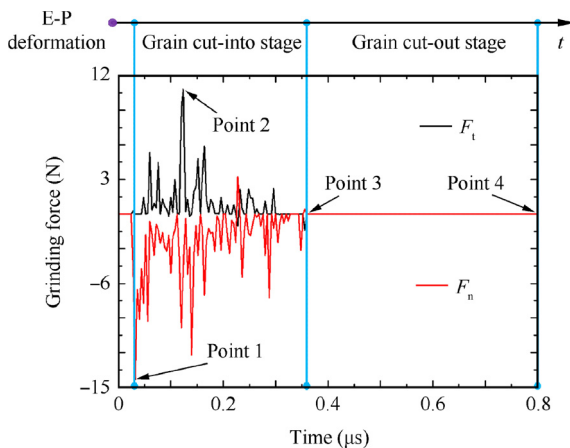| Parameter	Value
MGCD a_{gmax} (mm)	0.2, 0.4, 0.6, 0.8, 1.0
Depth of cut a_p (mm)	0.02
Grinding speed v_s (m/s)	40
Workpiece in-feed speed v_w (mm/min)	27.4, 54.7, 82.1, 109.4, 136.8
Grinding mode	Up grinding, water-based coolant

Fig.9 Time histories of grinding force.

sented in Table 3. Prior to grinding trials, the workpiece surfaces are polished by using the slurry with the abrasives (the abrasive sizes are #400, #800, and #1000) until the surface roughness Ra reaches 0.2 μm to keep grinding parameters (e.g., depth of cut) away from being influenced by the potential scratches on the workpiece surfaces.

The employed single-grit wheel is composed of three parts (see Fig. 7(a)), namely, (i) dummy wheel hub, (ii) dynamic balance block, and (iii) single-grit unit. For the single-grit unit (see Fig. 7(b)), a PCBN abrasive grain (see Fig. 7(c)) with abrasive size of #100 is fixed on the holding unit by using a high-frequency inductive brazing device.

All trials are performed on the surface grinder (MT-408, Blohm) by using the aforementioned single-grit wheel. A coolant supply with nozzle outlet pressure of 15 MPa and flowrate of 90 L/min is utilized to minimize the thermal effects on the experimental results. An acoustic-emission-based monitoring system (AE6000, Dittel) is employed to make the PCBN abrasive grain preset precisely to achieve accurate control of the grain cut depths.

After each grinding pass of the single-grit grinding operations, the 2D/3D morphologies of the PCBN abrasives are observed using a 3D microscope (KH-7700, Hirox) and a scanning electron microscope (SEM, S-3400, Hitachi).

3.2. Grinding parameter details

MGCD (refer to a_{gmax} in Fig. 8) is the key micro grinding parameter in the single-grit trials because it directly influences the grain–workpiece micro interactions and abrasive fracture/wear behavior. In the set of trials in this study, MGCD values are controlled by (i) zeroing the grain–workpiece contact plane and (ii) adjusting the macro grinding parameters (see Table 4) to achieve the desired a_{gmax} values according to the relationship given in Eq. (8).[48]

$$a_{gmax} = 2\lambda \frac{v_w}{v_s} \sqrt{\frac{a_p}{d_s}} \qquad (8)$$

where λ is the equivalent distance between two neighboring active grains (here, treating $\lambda = \pi d_s$ due to the single-grit wheel structure), v_w is the workpiece in-feed speed, v_s is the grinding speed, a_p is the depth of cut, and d_s is the wheel diameter.

4. Results and discussion

4.1. Fracture process analysis of PCBN abrasive grain

The detailed grinding process in the FE simulation is illustrated to ensure an in-depth comprehension for the convenience of later analysis of the fracture behavior of PCBN abrasive grain with various grinding parameters.
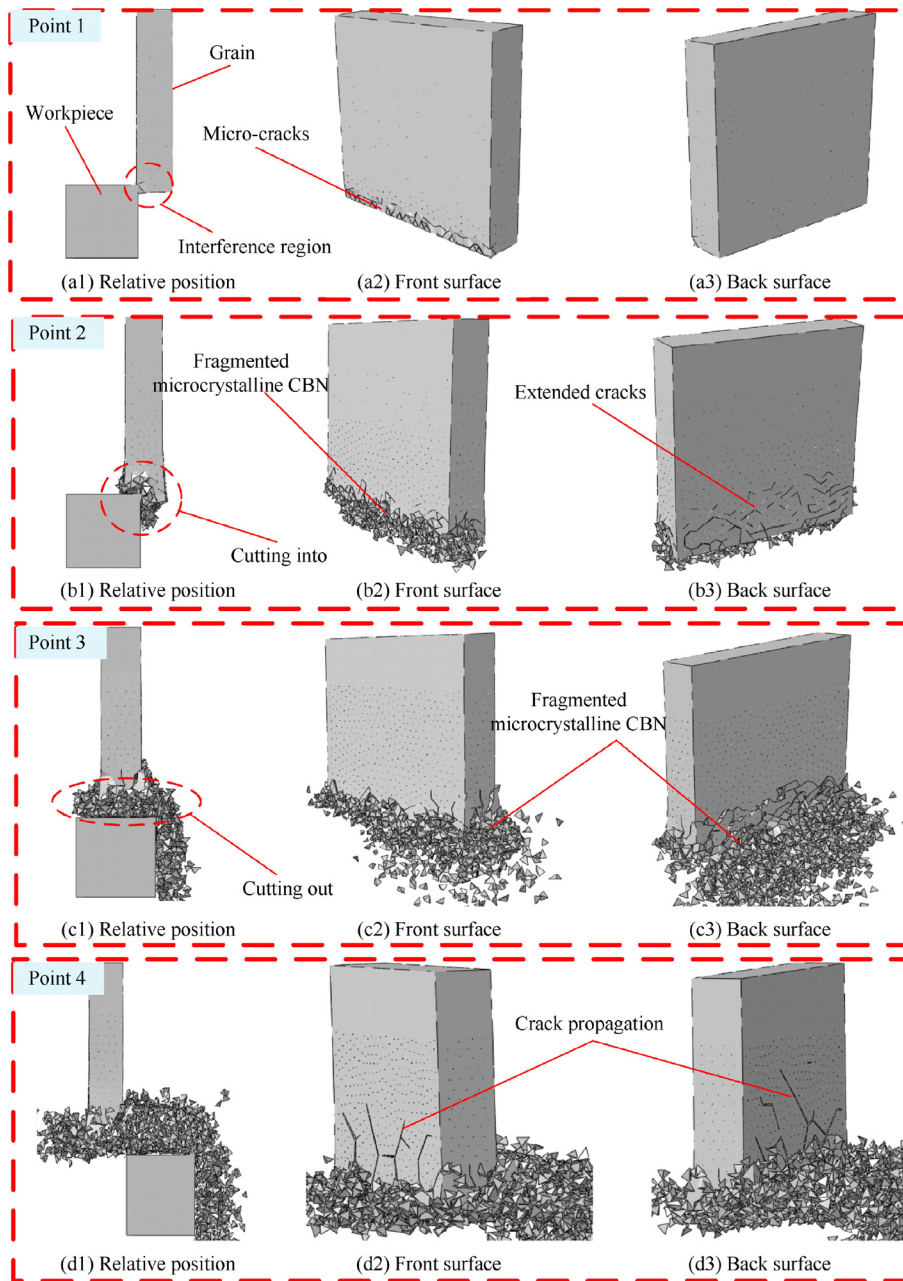
Fig. 10   Fracture morphology evolution of PCBN abrasive grain during grinding.

4.1.1. Fracture morphology and grinding force

Fig. 9 shows the time histories of grinding force when the PCBN abrasive grain cuts into and out of the workpiece with an MGCD of 0.2 μm and a grinding speed of 40 m/s. Fig. 10 presents the fracture morphology evolution of the PCBN abrasive grain that corresponds to the grinding moment at Points 1–4 labeled in Fig. 9.

Fig. 9 illustrates that the normal grinding force F_n and tangential grinding force F_t fluctuate seriously, which may be attributed to the fracture behavior of PCBN abrasive grains that generate random instantaneous grain–workpiece interactions during grinding. When the workpiece starts to contact the grain, the grinding force rapidly increases. Once the PCBN abrasive grain fractures, the grinding force decreases due to the temporary non-interaction. As the grinding process continues with the newly exposed grain interacting with the workpiece, the grinding force increases again.

The force history (see Fig. 9) demonstrates that the grinding process can be separated into three stages, namely, (i) elastic–plastic (E–P) deformation of PCBN abrasive grain before fracture, (ii) grain cut-in stage, and (iii) grain cut-out stage.

In stage (i), the PCBN abrasive grain begins to interact with the workpiece in the horizontal direction. As the workpiece moves further toward the grain, the E–P deformation happens at the grain bottom. At the grinding moment Point 1 (see Fig. 9), the tangential grinding force reaches the maximum value of 14.3 N although the grain–workpiece interference area is relatively small. As presented in Fig. 10(a2), microcracks
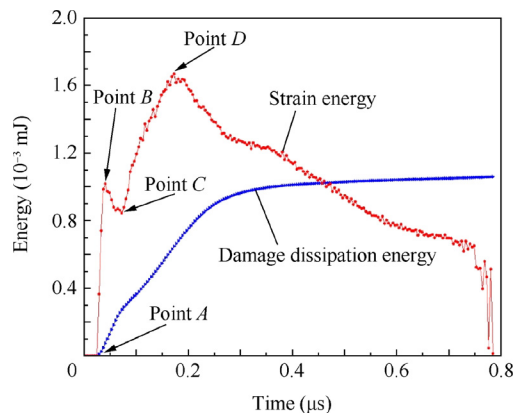
Fig. 11 Time histories of strain energy and damage dissipation energy inside PCBN abrasive grain.

appear on the front surface of the PCBN abrasive grain bottom but none on the back surface (see Fig. 10(a3)). The normal grinding force at this stage remains zero because no grain–workpiece interaction occur along the vertical direction.

Once the PCBN abrasive grain reaches the maximum E–P deformation (Point 1) in the horizontal direction, the grain starts to fracture and cuts into the workpiece. The tangential grinding force decreases due to the reduced interaction force owing to the fracture behavior of the PCBN abrasive grain. The fragmented microcrystalline accumulates in front of or above the workpiece (see Fig. 10(b1)) as the grain cuts into the workpiece. The interference appears along the vertical direction, together with the increase in the normal grinding force. When approaching Point 2, the normal grinding force reaches its maximum of 10.8 N in the entire grinding process. At this moment, half of the PCBN abrasive grain cuts into the workpiece with its front surface covered with fragmented microcrystalline CBN (see Fig. 10(b2)) and its back surface covered with the extended cracks (see Fig. 10(b3)). Later, both the normal grinding force and tangential grinding force decrease with the reduced thickness of the nonfragmented PCBN abrasive grain. When approaching Point 3, F_n and F_t reach zero, which indicates that the PCBN abrasive grain no longer interacts with the workpiece along the horizontal or vertical direction. This phenomenon is confirmed by Fig. 10(c1), which shows that not only the front surface of the PCBN abrasive grain but also the back surface are crowded with fragmented microcrystalline CBN (see Fig. 10(c2) and (c3)), and the bottom of the grain has totally cut into the workpiece.

As the workpiece moves away from the grain, the fragmented microcrystalline CBN concentrated in the non-interaction region starts to spread around the workpiece (see Fig. 10(d1)). When approaching Point 4, the PCBN abrasive grain cuts out the workpiece completely, and the entire grinding process ends.

The fracture region of the PCBN abrasive grain stays in the interaction part with the workpiece (according to our observation of Points 1–3). However, when the grain no longer squeezes with the workpiece after Point 3, the new cracks still extend (according to our observation of Point 4). This phenomenon can be explained by the fact that a mass of strain energy accumulates inside the PCBN abrasive grain due to the interaction with the workpiece. Although the grinding process finishes, the accumulated strain energy should be released. Therefore, some of them transform into the surface energy and the damage dissipation energy of newly emerging cracks.

4.1.2. Strain energy and damage dissipation energy

Fig. 11 shows the time histories of the strain energy and the damage dissipation energy inside the PCBN grain with an MGCD of 0.2 μm and a grinding speed of 40 m/s. The strain energy and damage dissipation energy inside the PCBN abrasive grain maintain their value of zero before Point A, which is attributed to the slight interaction between the grain and workpiece at the initial stage of the grinding process. At this moment, the E–P deformation of the PCBN abrasive grain does not occur, which is also consistent with the grinding force value of zero presented in Fig. 9.

In the period of Points A to B, the PCBN abrasive grain starts to squeeze with the workpiece in the horizontal direction. The strain energy increases rapidly to 1.0198×10^{-3} mJ, which indicates the high E–P deformation. The damage dissipation energy inside the PCBN abrasive grain also increases with the development of E–P deformation, which can be confirmed by the appearance of surface microcracks (see Fig. 10(a2)). The PCBN abrasive grain has not cut into the workpiece at this moment.

As the grinding process goes on, the PCBN abrasive grain starts to cut into the workpiece, and the squeezing action also occurs in the vertical direction. However, the strain energy decreases to 0.8619×10^{-3} mJ (at Point C) for a short time due to the temporary interaction gap caused by the initial fracture behavior of PCBN abrasive grain. The new cross section of the PCBN abrasive grain continues to interact with the workpiece and fractures constantly until it completely cuts into the workpiece. The strain energy reaches its maximum value of
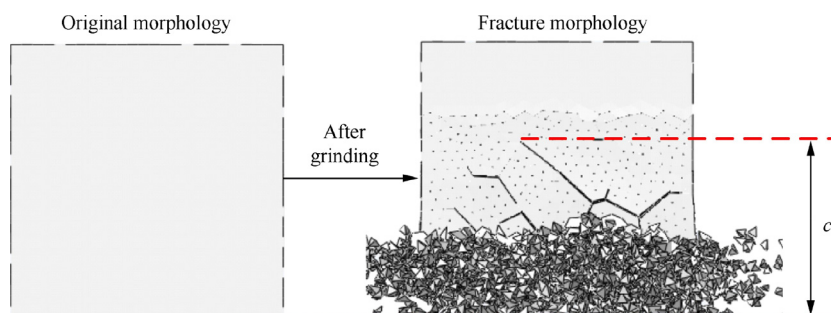

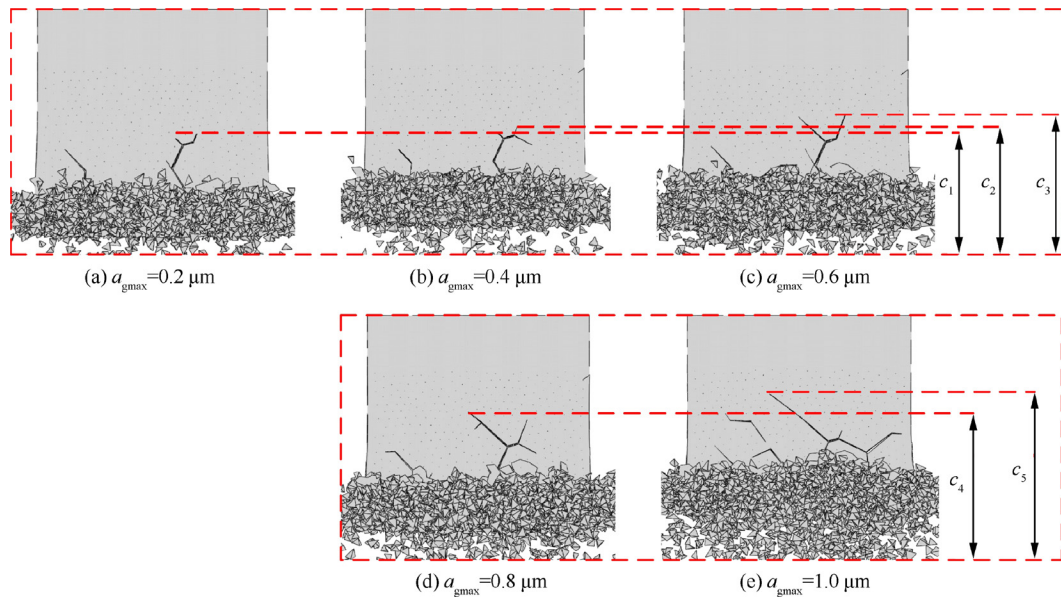**Fig. 12** Definition of PCBN abrasive grain fracture behavior scale.

Fig. 13   Fracture morphologies of PCBN abrasive grain with different MGCDs.
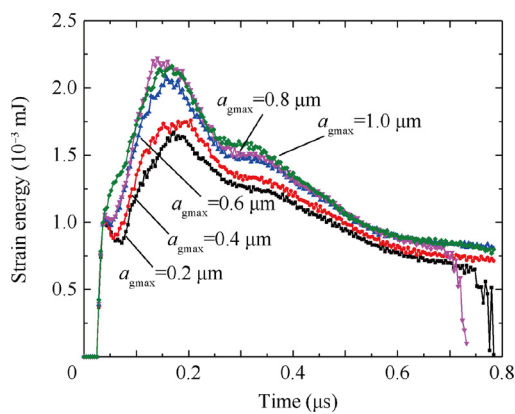

Fig. 14   Time histories of strain energy inside PCBN abrasive grain with different MGCDs (a_{gmax}).
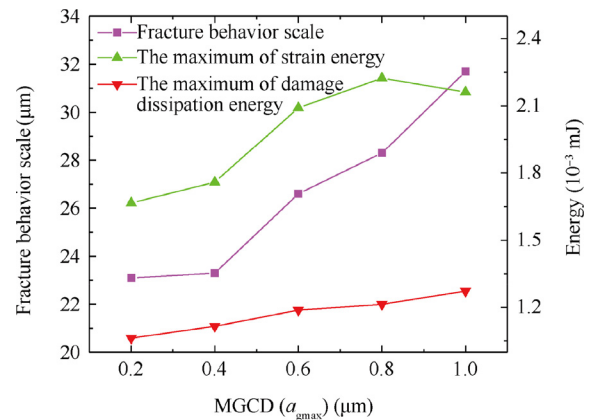

Fig. 16   Maximum of strain energy, maximum of damage dissipation energy of PCBN abrasive grain, and fracture behavior scale c with different MGCDs.
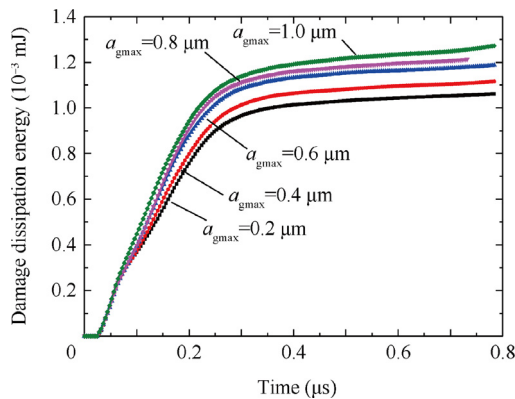

Fig.15   Time histories of damage dissipation energy of PCBN abrasive grain with different MGCDs (a_{gmax}).

1.6559×10^{-3} mJ at Point D. In the period of PCBN abrasive grain cutting into the workpiece, the damage dissipation energy increases at a high velocity, which can be observed from the fierce fracture behavior of the PCBN abrasive grain in Fig. 10(b2)–(b3). After Point D, the strain energy decreases due to the E–P recovery caused by the reduced interaction between the PCBN abrasive grain and workpiece. At the same time, a part of the strain energy accumulated in the PCBN abrasive grain is transformed into the damage dissipation energy. Consequently, crack propagation occurs in the upper surface of the PCBN abrasive grain, and the damage dissipation energy continues to increase at a low velocity.

4.1.3. Definition of fracture behavior scale

As described above, the grinding force can reflect the fracture evolution of the PCBN grain during grinding. The strain
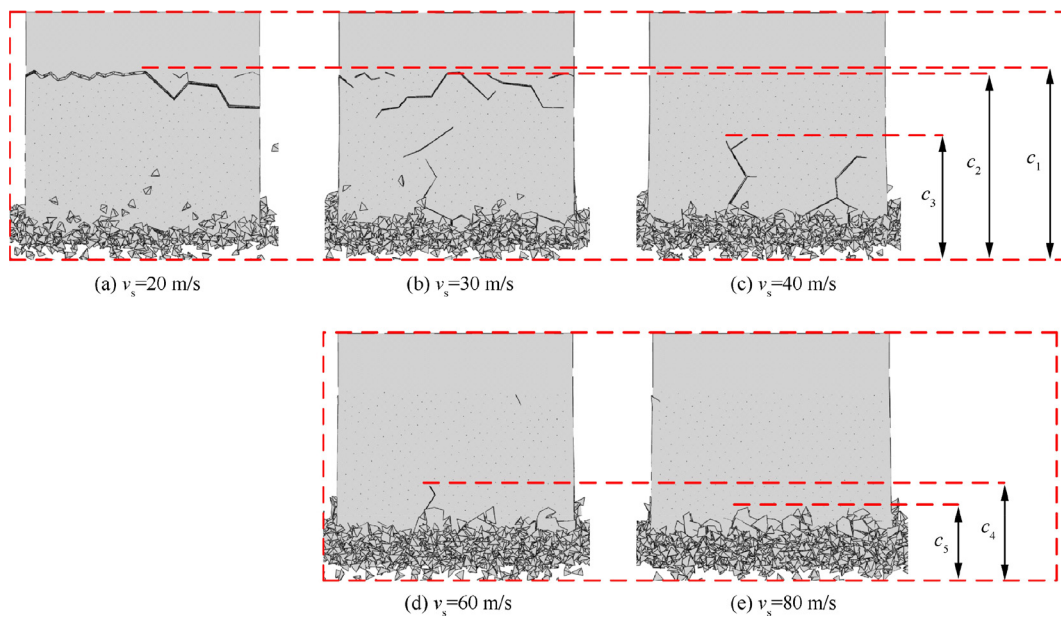
Fig. 17 Fracture morphologies of PCBN abrasive grain with different grinding speeds.
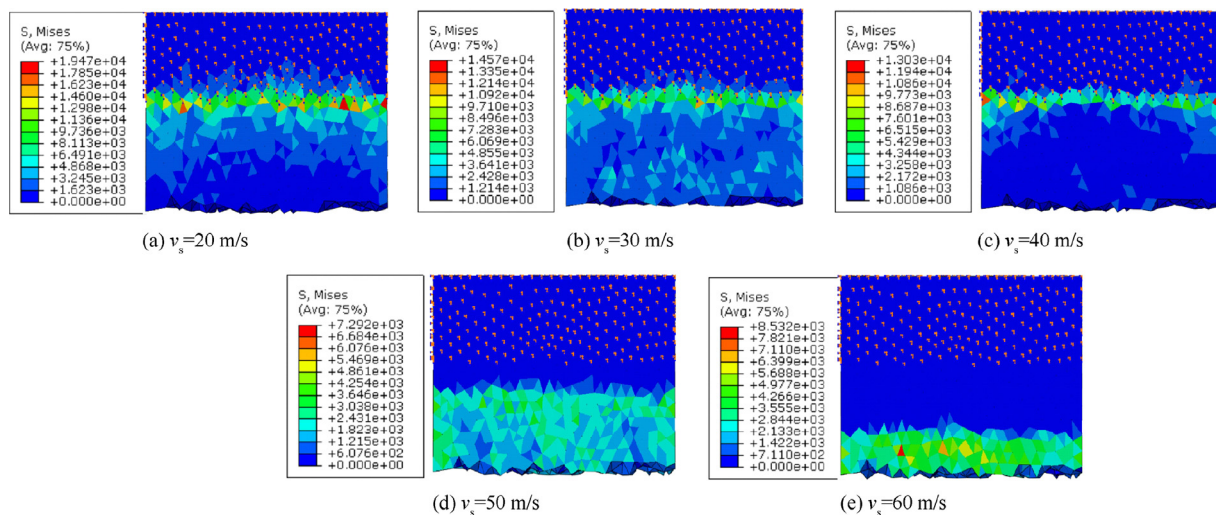

Fig. 18 Mises stress contours of PCBN abrasive grain with different grinding speeds.
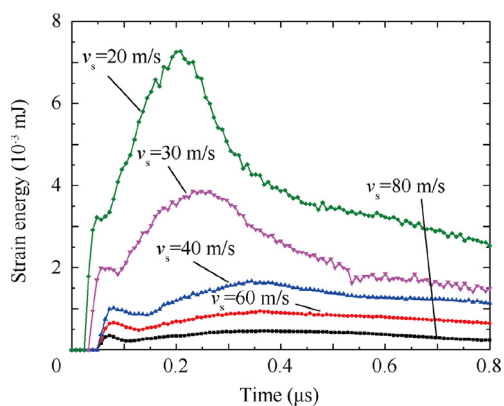

Fig. 19 Time histories of strain energy inside PCBN abrasive grain with different grinding speeds (v_s).

energy and damage dissipation energy inside the PCBN grain can indicate the E–P deformation and crack propagation degree. However, the fracture scale of the PCBN abrasive grain still needs to be quantitatively evaluated. A detailed parameter c, which represents the distance between the deepest crack tip and the bottom of the PCBN abrasive grain, is therefore defined (see Fig. 12).

4.2. Effects of grinding parameters on fracture behavior of PCBN abrasives

4.2.1. Effect of MGCD on fracture behavior of PCBN abrasives

The effect of MGCD (a_{gmax}) on the fracture behavior of the PCBN abrasive grain is investigated by using a constant grinding speed of 40 m/s and different MGCD values, including 0.2, 0.4, 0.6, 0.8, and 1.0 μm. Fig. 13 shows the fracture morphologies and crack propagation of the PCBN abrasive grain. The
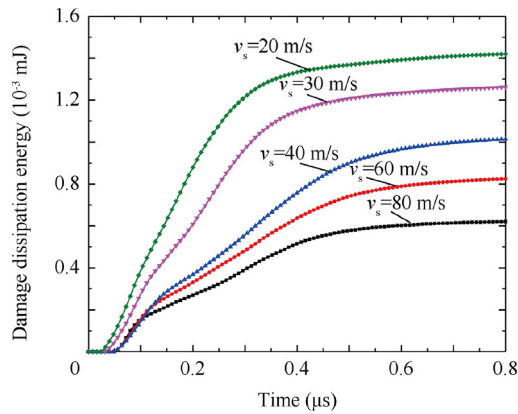
Fig. 20 Time histories of damage dissipation energy of PCBN abrasive grain with different grinding speeds (v_s).
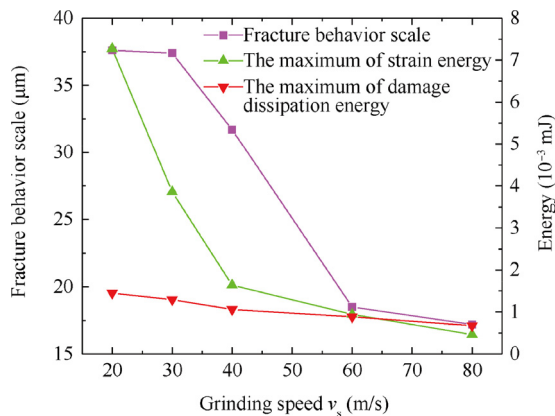

Fig. 21 Maximum of strain energy, maximum of damage dissipation energy of PCBN grain, and fracture behavior scale c with different grinding speeds.

contact area of the PCBN grain with workpiece gradually increases with increasing MGCD values, which causes the increase of fracture behavior scale (see c1, c2, c3, c4, and c5 labeled in Fig. 13).

Fig. 14 shows the time histories of the strain energy inside the PCBN abrasive grains with different values of MGCD. The value of strain energy also increases as the MGCD increases, which indicates that the E–P deformation and fracture behavior of the PCBN abrasive grain intensify at the same grinding moment. When the MGCD value increases from 0.4 μm to 0.6 μm, the increasing range of the strain energy values is the largest in comparison with its value when increasing from 0.2 μm to 0.4 μm or from 0.6 μm to 0.8 μm.

Fig. 15 shows the time histories of the damage dissipation energy of PCBN abrasive grains with different MGCDs. As introduced in Subsection 4.1.3, the damage dissipation energy value of PCBN abrasive grain reflects its fracture behavior scale. The slope of damage dissipation energy curve increases with the enlargement of MGCDs, which indicates that the damage dissipation energy growth rate and crack propagation rate of the PCBN abrasive grain enlarge continuously.

The maximum values of strain energy and damage dissipation energy in the entire grinding simulation and the fracture behavior scales (c1, c2, c3, c4, and c5) obtained after the grinding simulation are plotted in Fig. 16 for a detailed comparison and deep comprehension of PCBN abrasive grains with the same grinding speed but different MGCDs. The strain energy and damage dissipation energy increase with increasing MGCD values. The increment in the maximum strain energy value is 0.1029×10^{-3} mJ when the MGCD increases from 0.2 μm to 0.4 μm, and the increment is 0.3327×10^{-3} mJ from 0.4 μm to 0.6 μm, which is nearly three times that in the range of 0.2 μm to 0.4 μm. Similarly, the increment in the maximum damage dissipation energy value remains smaller than that in other ranges. The fracture scale only adds 0.2 μm when the MGCD increases from 0.2 μm to 0.4 μm, which is extremely small compared with that in other ranges (e.g., 3.3 μm when the MGCD increases from 0.4 μm to 0.6 μm). This result could lead to the conclusion that the ideal MGCD values range from 0.2 μm to 0.4 μm during the grinding simulation to minimize the micro fracture behavior and enhance the self-sharpening characteristics of PCBN abrasive grains.

4.2.2. Effect of grinding speed on fracture behavior of PCBN abrasives

Five different values of grinding speeds (20, 30, 40, 60, and 80 m/s) are also selected in the grinding simulation when the MGCD remains 0.2 μm. As the grinding speed increases, the PCBN abrasive grain fracture regions narrow (see c1, c2, c3, c4, and c5 labeled in Fig. 17), and the stress concentration region shrinks with increasing grinding speeds (see Fig. 18). When the grinding speed varies from 20 m/s to 40 m/s, the apparent stress concentration distributes from the bottom to the fixed part (corresponding to the brazed region of the PCBN abrasive grain), and the relating maximum stress values of the PCBN abrasive grain are 19470, 14570, and 13030 MPa. However, once the grinding speed is more than 60 m/s, the stress concentration region only appears at the bottom of the PCBN abrasive grain (far from the brazed region), which shows good concurrence with the fracture region presented in Fig. 17(e).

Fig. 19 shows the time histories of the strain energy inside the PCBN abrasive grains under different grinding speeds, and Fig. 20 shows the time histories of damage dissipation energy of the PCBN abrasive grains with different grinding speeds. Subsection 4.1 explains that the major fracture behavior of the PCBN grain in the grinding simulation concentrates on stage (ii) when the PCBN abrasive grain cuts into the workpiece. Therefore, Figs. 19 and 20 capture the first 0.8 μs of the entire grinding process. These figures illustrate that the strain energy and damage dissipation energy decrease with increasing grinding speeds. When the grinding speed varies from 20 m/s to 60 m/s, the strain energy and damage dissipation energy decrease considerably, which means that the E–P deformation of PCBN abrasive grains and the fracture behavior decrease significantly.

Fig. 21 shows the maximum values of the strain energy and damage dissipation energy of PCBN grains and the fracture behavior scale c under the condition that the MGCD values are set to 0.2 μm but with different grinding speeds. According to Fig. 21, the maximum values of the strain energy are 7.2726×10^{-3}, 3.8581×10^{-3}, 1.6704×10^{-3}, 0.9450×10^{-3}, and 0.4590×10^{-3} mJ when the grinding speed varies from
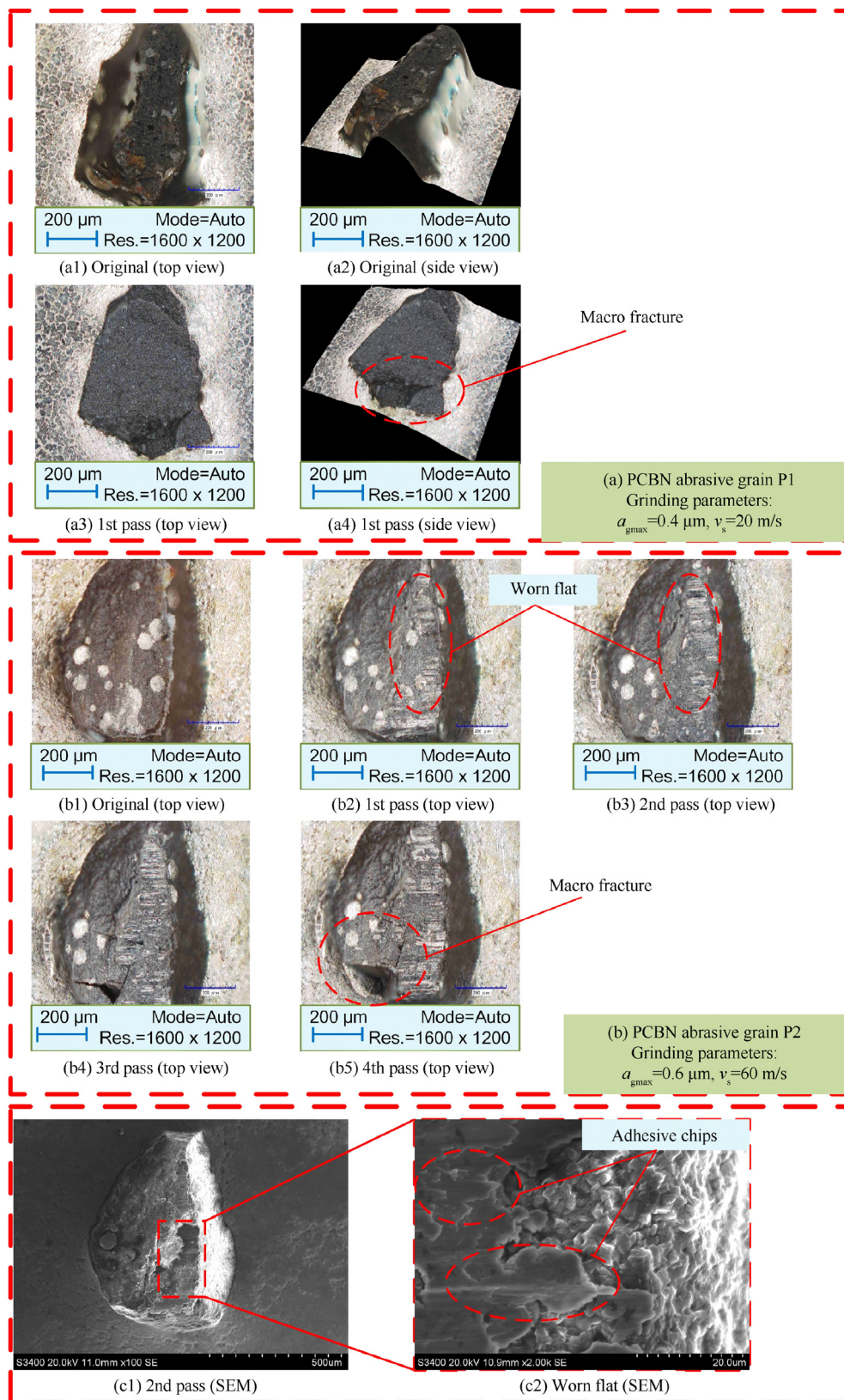
Fig. 22 Micrographs of PCBN abrasive grain (P1 and P2) surface morphologies after different passes.
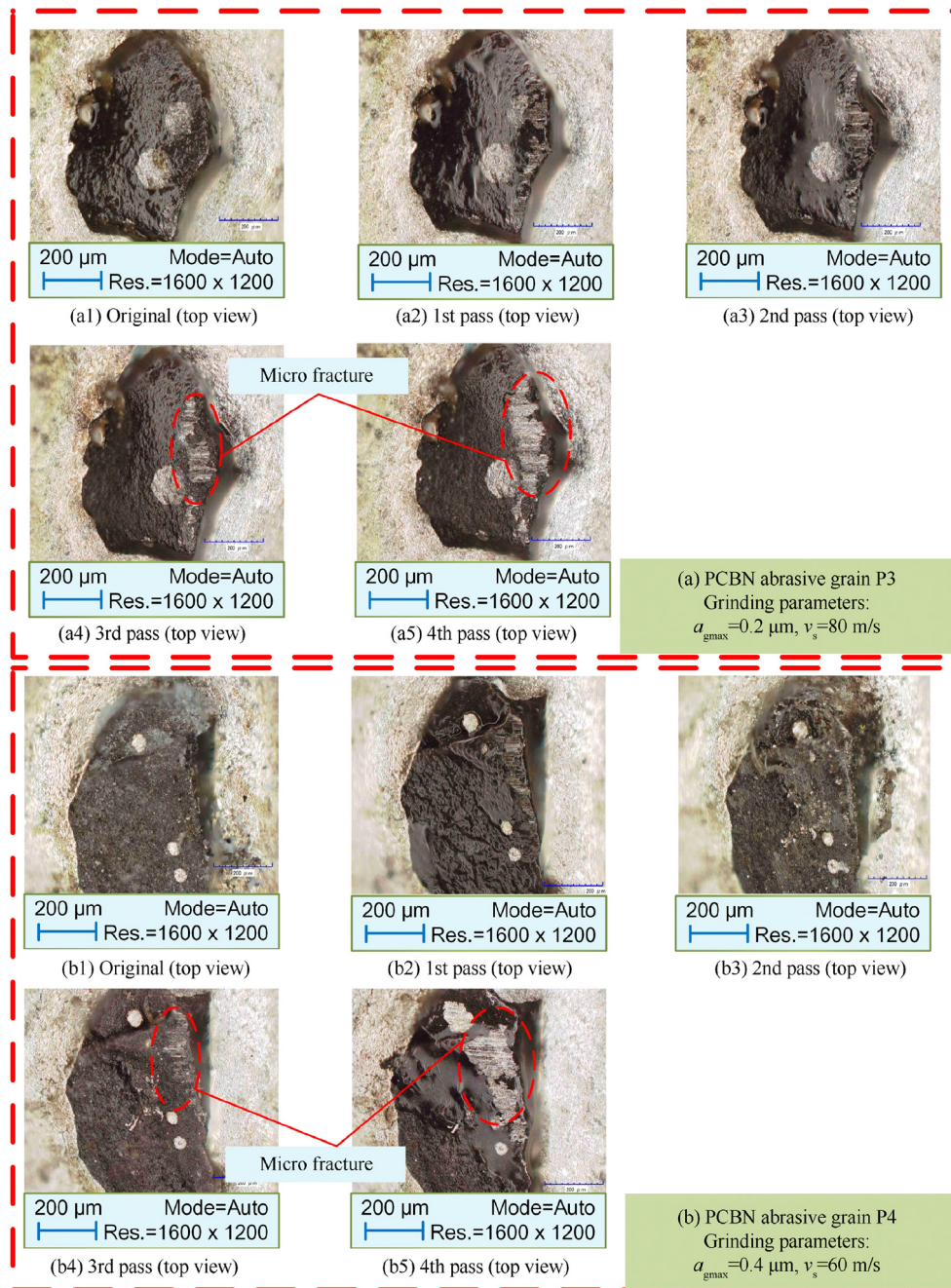
Fig. 23   Micrographs of PCBN abrasive grain (P3 and P4) surface morphologies after different passes.

20 m/s to 80 m/s, and the maximum values of damage dissipation energy are 1.4199×10^{-3}, 1.2625×10^{-3}, 1.0135×10^{-3}, 0.8246×10^{-3}, and 0.6199×10^{-3} mJ. When the grinding speed increases from 20 m/s to 30 m/s, the maximum value of strain energy decreases by 3.4145×10^{-3} mJ, whereas the maximum value of strain energy decreases only by 0.7254×10^{-3} mJ when increasing from 40 m/s to 60 m/s. A similar phenomenon also happens to the maximum value of damage dissipation energy, which indicates that the fracture behavior of the PCBN abrasive grain remains small when the grinding speed is over 60 m/s. The fracture behavior scales of the PCBN abrasive grains with the grinding speed varying from 20 m/s to 80 m/s are 37.6, 37.4, 31.7, 18.5, and 17.2 μm.

Thus, the fracture behavior scale of the PCBN abrasive grain remains small when the grinding speed is more than 60 m/s. In conclusion, according to the analyzed data, the PCBN abrasives are prone to participating in the grinding process with high grinding speed.

4.3. Grinding parameter optimization and experimental verification

From Section 4.2, the optimum MGCD should range from 0.2 μm to 0.4 μm and the grinding speed should be more than 60 m/s to reduce the fracture behavior scale of the PCBN abrasive grain during the grinding simulation. To validate

this finding, two groups of grinding parameters, which are out of the optimum range, are selected to perform the grinding experiments. Fig. 22 shows the surface wear morphologies of the PCBN abrasive grain P1 after different passes when the grinding speed is set as 20 m/s and the MGCD is 0.4 μm and the PCBN grain P2 with a grinding speed of 60 m/s and an MGCD of 0.6 μm. From Fig. 22(a), the macro fracture behavior (see Fig. 22(a4)) occurs on the root of the PCBN abrasive grain only after the first pass. The PCBN abrasive grain P1 consequently fails to participate in the following passes. From the macroscopic view, the wear mode of the PCBN grain P2 is mainly abrasion wear (see Fig. 22(b2)–(b3)), and the worn flat expands in the first two passes. From the micro view level (see Fig. 22(c2)), the worn flat occurs on the rear face of the PCBN abrasive grain P2 that is unsmooth. Numerous new outcropped micro-CBN particles distribute on the worn flat, which means that the wear feature of the PCBN abrasive grain P2 is micro fracture at this moment. However, after passes 3 and 4, macro fracture occurs in the lower left corner of the PCBN abrasive grain (see Fig. 22(b5)). In conclusion, macro fracture behavior happens easily on the PCBN abrasive grains if the grinding parameter is out of the optimum range.

The PCBN abrasive grains P3 and P4, which have diameters and surface morphologies similar to those of the PCBN grains P1 and P2, are selected to perform the contrast experiments. Unlike the grinding parameters of P1 and P2, those of P3 and P4 are in the optimum range obtained on the basis of the grinding simulation results. The PCBN grain P3 takes four passes with an MGCD of 0.2 μm and a grinding speed of 80 m/s, and P4 takes the same four passes with an MGCD of 0.4 μm and a grinding speed of 60 m/s. Fig. 23 shows the surface morphologies of the PCBN abrasive grains P3 and P4 after different passes. The local micro fracture behavior occurs at the top right corner of P3, together with the superior posterior of P4 after the third pass (see Fig. 23(a4), (b4)). No macro fracture behavior occurs for P3 or P4 in the entire grinding process after the four passes.

5. Conclusion

(1) Based on the cohesive element theory and Voronoi diagram, a finite element model of PCBN grain was established to simulate the fracture behavior in grinding. Furthermore, the FE model was testified reliably through the grinding experiments with single abrasive grain.

(2) The optimum range of the MGCD is 0.2–0.4 μm, within which the fracture behavior scale of PCBN abrasives can be minimised to enhance the promising self-sharpening ability of PCBN superabrasives. Deeper cuts might easily result in severe macro fracture behavior, which may lead to the failure of PCBN grains.

(3) The lowest critical grinding speed relating to PCBN abrasive fracture can be 60 m/s when the MGCD is kept as 0.2 μm. Lower speeds might easily lead to unexpected abrasive breakage, whereas higher speeds seem to be positive for an improved self-sharpening effect.

References

1. Ichida Y, Fujimoto M, Inoue Y. Development of a high performance vitrified grinding wheel using ultrafine-crystalline cBN abrasive grains. *J Adv Mech Design Syst Manuf* 2009;**4**(5):1005–14.
2. Mao C, Zhang MJ, Zhang J, Tang K, Gan HY, Zhang GF. The effect of processing parameters on the performance of spark plasma sintered cBN-WC-Co composites. *J Mater Eng Perform* 2015;**24**(12):4612–9.
3. Pal B, Chattopadhyay AK, Chattopadhyay AB. Development and performance evaluation of monolayer brazed cBN grinding wheel on bearing steel. *Int J Adv Manuf Technol* 2010;**48**(9):935–44.
4. Pal B, Chattopadhyay AK, Chattopadhyay AB. Performance study of brazed type cBN grinding wheel on hardened bearing steel and high speed steel. *Int J Precis Eng Manuf* 2012;**13**(5):649–54.
5. Mao C, Ren YH, Gan HY, Zhang MJ, Zhang J, Tang K. Microstructure and mechanical properties of CBN-WC-Co composites used for cutting tools. *Int J Adv Manuf Technol* 2015;**76**(9):2043–9.
6. Fujimoto M, Ichida Y. Micro fracture behavior of cutting edges in grinding using single crystal cBN grains. *Diam Relat Mater* 2008;**17**(7–10):1759–63.
7. Sunarto Ichida Y. Creep feed profile grinding of Ni-based superalloys with ultrafine-polycrystalline cBN abrasive grits. *Precis Eng* 2001;**25**(4):274–83.
8. Ding WF, Xu JH, Chen ZZ, Miao Q, Yang CY. Interface characteristics and fracture behavior of brazed polycrystalline CBN grains using Cu-Sn-Ti alloy. *Mater Sci Eng, A* 2013;**559**:629–34.
9. Ding WF, Xu JH, Chen ZZ. Grain wear of brazed polycrystalline CBN abrasive tools during constant-force grinding Ti–6Al–4V alloy. *Int J Adv Manuf Technol* 2011;**52**(9–12):969–76.
10. Miao Q, Ding WF, Xu JH. Fractal analysis of wear topography of brazed polycrystalline cBN abrasive grains during grinding nickel super alloy. *Int J Adv Manuf Technol* 2013;**68**(9–12):2229–36.
11. Zhu YJ, Ding WF, Huang X. Understanding the residual stress distribution in brazed polycrystalline CBN abrasive grains. *Int J Adv Manuf Technol* 2017;**88**(1–4):97–106.
12. Ding WF, Xu JH, Chen ZZ, Su HH, Fu YC. Wear behavior and mechanism of single-layer brazed CBN abrasive wheels during creep-feed grinding cast nickel-based superalloy. *Int J Adv Manuf Technol* 2010;**51**(5–8):541–50.
13. Sumiya H, Uesaka S, Satoh S. Mechanical properties of high purity polycrystalline cBN synthesized by direct conversion sintering method. *J Mater Sci* 2000;**35**(5):1181–6.
14. Suh CM, Bae KS, Suh MS. Wear behavior of diamond wheel for grinding optical connector ferrule-FEA and wear test. *J Mech Sci Technol* 2008;**22**(11):2009–15.
15. Mao C, Sun XL, Huang H, Kang CW, Zhang MJ, Wu YQ. Characteristics and removal mechanism in laser cutting of cBN-WC-10Co composites. *J Mater Process Technol* 2016;**230**:42–9.

16. Zhang Y, Li C, Ji H. Analysis of grinding mechanics and improved predictive force model based on material-removal and plastic-stacking mechanisms. *Int J Mach Tools Manuf* 2017;**122**:67–83.

17. Akbari M, Buhl S, Leinenbach C, Spolenak R, Wegener K. Thermomechanical analysis of residual stresses in brazed diamond metal joints using Raman spectroscopy and finite element simulation. *Mech Mater* 2012;**52**:69–77.

18. Zhu YJ, Ding WF, Yu TY, Xu JH, Fu YC, Su HH. Investigation on stress distribution and wear behavior of brazed polycrystalline cubic boron nitride superabrasive grains: numerical simulation and experimental study. *Wear* 2017;**376–377**:1234–44.

19. Turon A, Camanho PP, Costa J, Dávila CG. A damage model for the simulation of delamination in advanced composites under variable-mode loading. *Mech Mater* 2005;**38**(11):1072–89.

20. Chen GM, Chen JF, Teng JG. Behavior of FRP-to-concrete interfaces between two adjacent cracks: a numerical investigation on the effect of bondline damage. *Constr Build Mater* 2012;**28**(1):584–91.

21. Hillerborg A, Modéer M, Petersson PE. Analysis of crack formation and crack growth in concrete by means of fracture mechanics and finite elements. *Cem Concr Res* 1976;**6**:773–81.

22. Needleman A. A continuum model for void nucleation by inclusion debonding. *J Appl Mech* 1987;**54**(3):525–31.

23. Zhou TT, Huang CZ, Liu HL, Wang J, Zou B, Zhu HT. Crack propagation simulation in microstructure of ceramic tool materials. *Comput Mater Sci* 2012;**54**:150–6.

24. Mohadeseh S, Hosseinkhani B, Hosseinkhani B, Vieeillard C, Chambart M, Johannes Jozef Kok P, et al. On the influence of transgranular and intergranular failure mechanisms during dynamic loading of silicon nitride. *Acta Mater* 2014;**67**:239–51.

25. Wang ZY, Li PF. Voronoi cell finite element modelling of the intergranular fracture mechanism in polycrystalline alumina. *Ceram Int* 2017;**43**:6967–75.

26. Zhou TT, Huang CZ. Simulation of crack propagation in single phase ceramic tool materials. *Comput Mater Sci* 2015;**104**:177–84.

27. Alveen P, McNamara D, Carolan D. The influence of microstructure on the fracture statistics of polycrystalline diamond and polycrystalline cubic boron nitride. *Comput Mater Sci* 2015;**109**:115–23.

28. Simonovski I, Cizelj L. Cohesive zone modeling of intergranular cracking in polycrystalline aggregates. *Nucl Eng Des* 2015;**283**:139–47.

29. Yao Y, Liu L, Keer LM. Pore pressure cohesive zone modeling of hydraulic fracture in quasi-brittle rocks. *Mech Mater* 2015;**83**:17–29.

30. Ding WF, Xu JH, Chen ZZ, Su HH, Fu YC. Effects of heating temperature on interfacial microstructure and compressive strength of brazed CBN-AlN composite abrasive grits. *J Wuhan Univ Technol Mater Sci Ed* 2010;**25**(6):952–6.

31. Mckie A, Winzer J, Sigalas I, et al. Mechanical properties of cBN-Al composite materials. *Ceram Int* 2011;**37**(1):1–8.

32. Zhang P, Balint D, Lin J. An integrated scheme for crystal plasticity analysis: Virtual grain structure generation. *Comput Mater Sci* 2011;**50**(10):2854–64.

33. Zhang P, Karimpour M, Balint D, Lin JG, Farrugia D. A controlled Poisson Voronoi tessellation for grain and cohesive boundary generation applied to crystal plasticity analysis. *Comput Mater Sci* 2012;**64**:84–9.

34. Warner DH, Molinari JF. Micromechanical finite element modeling of compressive fracture in confined alumina ceramic. *Acta Mater* 2006;**54**(19):5135–45.

35. Sfantos GK, Aliabadi MH. A boundary cohesive grain element formulation for modelling intergranular microfracture in polycrystalline brittle materials. *Int J Numer Methods Eng* 2007;**69**(8):1590–626.

36. Zhu HX, Thorpe SM, Windle AH. The geometrical properties of irregular two-dimensional Voronoi tessellations. *Philos Mag* 2001;**81**(12):2765–83.

37. Huang X, Ding WF, Zhu YJ, Yang CY. Influence of microstructure and grinding load on the bulk toughness and fracture behavior of PCBN abrasive grains. *Int J Adv Manuf Technol* 2018;**94**(9–12):4519–30.

38. Dugdale DS. Yielding of steel sheets containing slits. *J Mech Phys Solids* 1960;**8**:100–4.

39. Barenblatt GI. The mathematical theory of equilibrium cracks in brittle fracture. *Adv Appl Mech* 1962;**7**:55–129.

40. Jiang WG, Hallett Stephen R. A concise interface constitutive law for analysis of delamination and splitting in composite materials and its application to scaled notched tensile specimens. *Int J Numer Methods Eng* 2007;**69**(9):1982–95.

41. Carolan D, Alveen P, Ivanković A, Murphy N. Effect of notch root radius on fracture toughness of polycrystalline cubic boron nitride. *Eng Fract Mech* 2011;**78**(17):2885–95.

42. Li GX, Yi S, Sun SJ, Ding SL. Wear mechanisms and performance of abrasively ground polycrystalline diamond tools of different diamond grains in machining titanium alloy. *J Manuf Processes* 2017;**29**:320–31.

43. Zhang ZY, Du YF, Wang B, Wang ZG, Kang RK, Guo DM. Nanoscale wear layers on silicon wafers induced by mechanical chemical grinding. *Tribol Lett* 2017;**65**(4):132.

44. Zhang ZY, Huang SL, Wang SC, et al. A novel approach of high-performance grinding using developed diamond wheels. *Int J Adv Manuf Technol* 2017;**91**(9–12):3315–26.

45. Zhang ZY, Guo DM, Wang B, Kang RK, Zhang B. A novel approach of high speed scratching on silicon wafers at nanoscale depths of cut. *Sci Rep* 2015;**5**:16395.

46. Wang B, Zhang ZY, Chang KK, et al. New deformation-induced nanostructure in silicon. *Nano Lett* 2018;**18**(7):4611–7.

47. Zhang ZY, Wang B, Kang RK, Zhang B, Guo DM. Changes in surface layer of silicon wafers from diamond scratching. *CIRP Ann Manuf Technol* 2015;**64**(1):349–52.

48. Malkin S, Guo C. *Grinding technology: theory and applications of machining with abrasives*. 2nd ed. New York: Industrial Press; 2001.